

The DIVING^{3D} Survey – Deep IFS View of Nuclei of Galaxies – I. Definition and Sample Presentation

J. E. Steiner¹★, R. B. Menezes²†, T. V. Ricci³‡, Patrícia da Silva¹§, R. Cid Fernandes⁴, N. Vale Asari^{4,5}¶, M. S. Carvalho⁴, D. May¹, Paula R. T. Coelho¹ and A. L. de Amorim⁴

¹Instituto de Astronomia, Geofísica e Ciências Atmosféricas, Departamento de Astronomia, Universidade de São Paulo, 05508-090, SP, Brazil

²Instituto Mauá de Tecnologia, Praça Mauá 1, 09580-900, São Caetano do Sul, SP, Brazil

³Universidade Federal da Fronteira Sul, Cerro Largo, 97900-000, RS, Brazil

⁴Universidade Federal de Santa Catarina, Departamento de Física–CFM, C.P. 476, 88040-900, Florianópolis, SC, Brazil

⁵University of St Andrews, School of Physics and Astronomy, North Haugh, St Andrews KY16 9SS, UK

Accepted XXX. Received YYY; in original form ZZZ

ABSTRACT

We present the Deep Integral Field Spectrograph View of Nuclei of Galaxies (DIVING^{3D}) survey, a seeing-limited optical 3D spectroscopy study of the central regions of all 170 galaxies in the Southern hemisphere with $B < 12.0$ and $|b| > 15^\circ$. Most of the observations were taken with the Integral Field Unit of the Gemini Multi-Object Spectrograph, at the Gemini South telescope, but some are also being taken with the Southern Astrophysical Research Telescope (SOAR) Integral Field Spectrograph. The DIVING^{3D} survey was designed for the study of nuclear emission-line properties, circumnuclear (within scales of hundreds of pc) emission-line properties, stellar and gas kinematics and stellar archaeology. The data have a combination of high spatial and spectral resolution not matched by previous surveys and will result in significant contributions for studies related to, for example, the statistics of low-luminosity active galactic nuclei, the ionization mechanisms in Low-Ionization Nuclear Emission-Line Regions, the nature of transition objects, among other topics.

Key words: galaxies: nuclei – galaxies: active – galaxies: Seyfert – techniques: imaging spectroscopy

1 INTRODUCTION

Galaxies have been known as entities containing hundreds of billions of stars – “islands in the universe” – for nearly a century. Their nuclei certainly preserve important information about their origin and evolution. For these reasons it is important to study them, both at the individual level and on a statistical basis. Many galactic nuclei present emission lines associated with the accretion of matter onto a central supermassive black hole (SMBH), with a mass in the range of 10^6 – $10^{10} M_\odot$. They are the so-called active galactic nuclei (AGNs). The luminosity function of AGNs is such that they can be studied at large distances. Curiously the most abundant objects are low luminosity AGNs (LLAGNs), which are not so well understood, despite their predominance in galaxies in the local Universe. The LLAGNs (as all AGNs) can be classified depending on the presence (type 1) or absence (type 2) of broad permitted emission lines. The detection of a broad component is considered a conclusive proof that the object contains an AGN and, therefore, a SMBH (see Netzer 2013 for a detailed discussion).

Most of the massive galaxies in the local Universe host an active nucleus (Ho 2008), the majority of them presenting low-

ionization emission lines and hence classified as Low-Ionization Nuclear Emission-Line Regions (LINERs; Heckman 1980). The nuclear emission in LINERs has been proposed to be similar to that of Seyfert galaxies, but in an environment with lower ionization parameter (Ferland & Netzer 1983; Halpern & Steiner 1983); this idea was confirmed by the discovery of broad H α emission in a significant fraction of LINERs (Ho et al. 1997) as well as the detection of optical non-thermal continuum (Maoz et al. 1995), high-ionization forbidden lines (Dudik et al. 2009) and compact central X-ray sources (González-Martín et al. 2009). Such characteristics are usually associated with AGNs. However it was also found that low-ionization emission can be quite extended in early-type galaxies (ETGs, Phillips et al. 1986; Sarzi et al. 2010), far beyond the ionization produced by a low-luminosity central source. The source of this ionization was proposed to be a population of hot low-mass evolved stars (HOLMES¹, Binette et al. 1994). In the last two decades significant evidence of nuclear activity has been detected in LINER galaxies (e.g. Nagar et al. 2005; Ho 2008; Masegosa et al. 2011; Heckman & Best 2014; Cazzoli et al. 2018); however, the evidence of extended HOLMES-ionized emission has also grown (e.g. Stasińska et al. 2008; Eracleous et al. 2010; Sarzi et al. 2010; Cid Fernandes et al. 2011; Yan & Blanton 2012; Singh et al. 2013; Belfiore et al. 2016). Approximately

★ Deceased

† roberto.menezes@maua.br

‡ tiago.ricci@uffs.edu.br

§ p.silva2201@gmail.com

¶ Royal Society–Newton Advanced Fellowship

¹ This term has been proposed by Flores-Fajardo et al. (2011); sometimes they are referred to as hot post-asymptotic giant branch stars, but it can also include nuclei of planetary nebulae and white dwarfs.

two thirds of E–Sb galaxies exhibit local weak nuclear activity incompatible with normal stellar processes; in contrast, only about 15 per cent of the Sc–Sm galaxies are known to have AGN activity (Ho 2008). Late type galaxies are generally of low mass, gas rich, with strong star formation, and are frequently characterized as having a central stellar cluster (Walcher et al. 2006; Bekki & Graham 2010). The nature of these clusters is still poorly understood and they are even considered as failed black holes (Neumayer & Walcher 2012).

It is now well established that there are correlations between the masses of central SMBHs and certain properties of the host galaxies, such as the bulge stellar velocity dispersion (the so-called M – σ relation; Ferrarese & Merritt 2000; Gebhardt et al. 2000; Gültekin et al. 2009), which has generated great interest in studying the connections between SMBH growth and galaxy formation/evolution. As a direct manifestation of accretion and growth, black holes have been considered as essential components of structure formation (Springel et al. 2005; Hopkins & Hernquist 2006; Granato et al. 2004).

An effective way of studying galaxies and their nuclei is by performing surveys of large samples. With such surveys, new and interesting objects can be found and, if the samples are selected by rigorous criteria, statistical properties can be derived. One of the most popular surveys of galactic nuclei was the PALOMAR survey (Filippenko & Sargent 1985; Ho 2008). This survey was based on single spectra taken with a $2 \text{ arcsec} \times 4 \text{ arcsec}$ slit on the Palomar 5 m telescope for every galaxy brighter than $B = 12.5$ in the Revised Shapley-Ames Catalog of Bright Galaxies (RSA, Sandage & Tammann 1981). A total of 486 galaxies was included in this survey.

Important and influential as it was (and still is), the PALOMAR survey offers no information on the spatial distribution of the light-emitting/-absorbing sources in the central region of galaxies. That requires 3D spectroscopy with a high spatial resolution. To overcome this issue, we present the Deep IFS View of Nuclei of Galaxies (DIVING^{3D}) survey, which uses seeing-limited optical 3D spectroscopy data to study the nuclear and circumnuclear regions (scales of $\sim 100 \text{ pc}$) of all 170 galaxies in the Southern hemisphere with $B < 12.0$ and $|b| > 15^\circ$. The combination of a statistical complete survey with such spatial scales is currently a unique opportunity to redraw the statistics of the ionization sources for LLAGNs.

The paper is organized as follows. In Section 2, we describe in detail the DIVING^{3D} survey and its main objectives. In Section 3, we present the methodologies used for the treatment and analysis of the observational data obtained for the survey. In Section 4, we show some of the early results obtained so far. Finally, we present a summary of all topics in Section 5.

Table 1: Parameters of the galaxies in the DIVING^{3D} sample.

Object	Type	B	M_B	Distance (Mpc)	Obs. Date	Grating	Exp. Time (s)
GMOS-North							
NGC 4030	SA(s)bc	11.07	-21.38	29.9 ^a	09/04/2013	R831-G5302	3×960
NGC 4697	E6	10.11	-20.4	12.4 ^a	09/04/2014	R831-G5302	3×960
NGC 4775	SA(s)d	11.74	-18.45	12 ^b	24/06/2016	R831-G5302	3×862
NGC 4781	SB(rs)d	11.69	-18.85	12.8 ^c	27/06/2016	R831-G5302	3×862
NGC 4981	SAB(r)bc	11.83	-19.54	19.4 ^c	24/06/2016	R831-G5302	3×862
NGC 5792	SB(rs)b	11.72	-20.23	25 ^c	23/06/2016	R831-G5302	3×862
NGC 7184	SB(r)c	11.67	-21.07	36.1 ^c	20/06/2016	R831-G5302	3×862
NGC 7314	SAB(rs)bc	11.65	-19.66	16 ^c	06/07/2016	R831-G5302	3×862
GMOS-South							
NGC 134	SAB(s)bc	10.96	-20.41	18.3 ^c	24/06/2015	R831-G5322	3×930
NGC 157	SAB(rs)bc	11.04	-19.64	12.9 ^d	23/12/2014	R831-G5322	3×930
NGC 247	SAB(s)d	9.51	-17.88	3.34 ^e	26/06/2015	R831-G5322	3×930
NGC 253	SAB(s)c	8.13	-19	3.05 ^e	07/10/2013	R831-G5322	3×910
NGC 289	SB(rs)bc	11.81	-20.07	21.6 ^c	26/09/2016	R831-G5322	3×866
NGC 300	SA(s)d	8.70	-17.38	2.17 ^c	26/08/2013	B600-G5323	1800
NGC 584	E4	11.20	-21.83	20 ^a	24/12/2013	B600-G5323	1800
NGC 596	cD	11.88	-20.28	21.7 ^a	24/12/2016	B600-G5323	3×565
NGC 613	SB(rs)bc	10.75	-21.02	21.4 ^f	25/01/2015	R831-G5322	3×930
NGC 720	E5	11.15	-21.63	30.7 ^g	11/08/2013	B600-G5323	1800
NGC 908	SA(s)c	10.87	-20.5	18.5 ^c	01/12/2014	R831-G5322	3×930
NGC 936	SB0(rs)	11.19	-20.71	19.9 ^h	24/11/2014	B600-G5323	3×630
NGC 1052	E4	11.53	-20.19	19.2 ^a	30/09/2013	B600-G5323	1800
NGC 1068	(R)SA(rs)b	9.55	-20.35	10.1 ^f	13/11/2010	B600-G5323	6×830
NGC 1097	SB(s)b	10.16	-20.71	15.4 ^c	10/08/2016	B600-G5323	3×565
NGC 1187	SB(r)c	10.93	-20.26	21.4 ^c	23/12/2014	R831-G5322	3×930
NGC 1201	SA0(r)	11.56	-19.97	20.2 ⁱ	02/10/2016	B600-G5323	3×565
NGC 1255	SAB(rs)bc	11.60	-19.19	14.1 ^c	29/12/2016	R831-G5322	3×866
NGC 1291	(R)SB0/a(s)	9.42	-19.99	8.6 ^j	27/11/2014	B600-G5323	3×630
NGC 1300	SB(rs)bc	11.10	-19.85	14.5 ^f	11/09/2013	B600-G5323	1800
NGC 1302	(R)SB0/a(r)	11.38	-18.48	8.36 ^b	07/01/2016	B600-G5323	3×565
NGC 1313	SB(s)d	9.37	-18.33	3.7 ^j	04/12/2012	B600-G5323	3×589
NGC 1316	SAB0(s)	9.60	-22.64	20.8 ^k	07/10/2013	B600-G5323	1800
NGC 1326	(R)SB0(r)	11.34	-20.29	18.9 ^l	28/09/2016	B600-G5323	3×565
NGC 1332	S0(s)	11.29	-20.68	22.9 ⁱ	07/10/2013	B600-G5323	1800
NGC 1344	E5	11.28	-20.53	21 ^m	01/10/2016	B600-G5323	3×565
NGC 1365	SB(s)b	10.21	-20.66	13.6 ^c	01/12/2014	B600-G5323	3×630
NGC 1380	SA0	11.10	-21	20.6 ^m	07/08/2008	B600-G5323	1800
NGC 1387	SAB0(s)	11.83	-19.93	19.1 ^a	14/01/2016	B600-G5323	3×565
NGC 1395	E2	11.18	-21.57	24.3 ^h	26/08/2013	B600-G5323	1800
NGC 1398	(R')SB(r)ab	10.60	-22.16	28.6 ^c	13/09/2015	B600-G5323	3×565
NGC 1399	E1	10.79	-21.67	21.1 ^m	04/08/2008	B600-G5323	1800
NGC 1404	E1	11.06	-20.81	19 ^g	05/08/2008	B600-G5323	1800
NGC 1407	E0	10.93	-21.87	25.1 ⁿ	26/08/2013	B600-G5323	1800
NGC 1411	SA0(r)	11.70	-19.92	19.1 ^a	15/01/2016	B600-G5323	3×565
NGC 1427	cD	11.94	-20.63	25.8 ^g	28/09/2016	B600-G5323	3×565
NGC 1433	(R')SB(r)ab	10.68	-19.26	8.32 ^e	20/01/2016	B600-G5323	3×565
NGC 1515	SAB(s)bc	11.93	-19.61	17.9 ^c	11/11/2016	R831-G5322	3×866
NGC 1527	SAB0(r)	11.70	-19.74	18.5 ^h	16/12/2015	B600-G5323	3×565
NGC 1533	SB0	11.71	-20.36	24.1 ^g	15/01/2016	B600-G5323	3×565
NGC 1537	SAB0	11.62	-20.39	23.1 ^a	15/01/2016	B600-G5323	3×565
NGC 1543	(R)SB0(s)	11.49	-20.81	18.4 ^g	20/01/2016	B600-G5323	3×565
NGC 1549	E0-1	10.76	-20.51	16.3 ^g	28/08/2013	B600-G5323	1800
NGC 1553	SA0(r)	10.42	-19.99	9.51 ^g	24/11/2014	B600-G5323	3×630
NGC 1559	SB(s)cd	10.97	-19.43	11.6 ^c	12/01/2014	R831-G5322	3×1000
NGC 1566	SAB(s)bc	10.21	-21.02	18 ^o	10/10/2013	R831-G5322	3×910
NGC 1574	SA0(s)	11.19	-20.69	20.1 ^h	28/08/2013	B600-G5323	1800
NGC 1617	SB(s)a	11.37	-19.48	13.4 ^j	01/10/2016	B600-G5323	3×565
NGC 1672	SB(s)b	11.03	-19.98	11.4 ^p	15/01/2016	B600-G5323	3×565
NGC 1700	E4	11.96	-20.65	33.1 ^g	04/11/2013	B600-G5323	1800
NGC 1792	SA(rs)bc	10.85	-19.37	10.8 ^c	20/12/2014	R831-G5322	3×930
NGC 1808	(R)SAB(s)a	10.70	-19.35	9.51 ^c	15/12/2015	B600-G5323	3×565
NGC 1947	S0	11.86	-20.37	19.6 ^q	15/12/2015	B600-G5323	3×565
NGC 2207	SAB(rs)bc	11.35	-21.54	36.1 ^q	10/11/2016	R831-G5322	3×866

Object	Type	B	M_B	Distance (Mpc)	Obs. Date	Grating	Exp. Time (s)
NGC 2217	(R)SB0(rs)	11.59	-20.91	25.6 ^g	11/10/2013	B600-G5323	1800
NGC 2442	SAB(s)bc	11.16	-20.99	20.1 ^r	23/02/2014	R831-G5322	3×815
NGC 2784	SA0(s)	11.21	-19.48	9.59 ^a	16/05/2013	B600-G5323	1800
NGC 2835	SB(rs)c	10.95	-18.82	8.75 ^a	12/05/2015	R831-G5322	3×865
NGC 2974	E4	11.78	-20.36	22.1 ^a	28/06/2013	B600-G5323	1800
NGC 2997	SAB(rs)c	10.32	-20.94	13.1 ^f	27/11/2013	R831-G5322	3×930
NGC 3115	S0	9.98	-20.17	9.68 ⁱ	30/06/2013	B600-G5323	1800
NGC 3223	SA(s)b	11.88	-21.54	37.5 ^c	07/02/2017	B600-G5323	3×560
NGC 3511	SA(s)c	11.56	-19.2	12.6 ^c	11/05/2015	R831-G5322	3×865
NGC 3513	SB(rs)c	11.99	-17.56	7.8 ^f	17/02/2018	R831-G5322	3×885
NGC 3557	E3	11.46	-21.07	26.8 ^g	16/06/2013	B600-G5323	1800
NGC 3585	E6	10.93	-20.27	13.1 ^g	16/05/2013	B600-G5323	1800
NGC 3621	SA(s)d	10.03	-19.29	6.4 ^c	22/02/2014	R831-G5322	3×815
NGC 3672	SA(s)c	11.66	-20.2	25.1 ^c	17/03/2017	R831-G5322	3×870
NGC 3887	SB(r)bc	11.60	-19.92	18.2 ^f	17/03/2017	R831-G5322	3×870
NGC 3904	E2-3	11.95	-20.81	28.3 ^a	11/05/2013	B600-G5323	1800
NGC 3923	E4-5	10.91	-20.86	16 ^g	14/05/2013	B600-G5323	1800
NGC 3962	E1	11.66	-21.49	36.3 ^a	29/06/2013	B600-G5323	1800
NGC 4105	E3	11.88	-20.79	26.7 ^a	01/07/2013	B600-G5323	1800
NGC 4487	SAB(rs)cd	11.66	-18.62	12.3 ^c	09/03/2017	R831-G5322	3×870
NGC 4504	SA(s)cd	11.92	-19.24	17.5 ^c	23/02/2018	R831-G5322	3×885
NGC 4546	SB0(s)	11.30	-19.46	14 ^a	17/02/2008	B600-G5323	1200
NGC 4593	(R)SB(rs)b	11.72	-20.92	37.2 ^q	02/03/2017	B600-G5323	3×560
NGC 4594	SA(s)a	9.28	-22.72	21.7 ^s	03/02/2011	B600-G5323	3×595
NGC 4666	SABc	11.56	-19.53	14 ^c	11/05/2015	R831-G5322	3×882
NGC 4691	(R)SB0/a(s)	11.70	-20.11	20.6 ^b	13/02/2015	B600-G5323	3×582
NGC 4696	cD1	11.59	-22.2	39.8 ⁿ	04/05/2013	B600-G5323	1800
NGC 4699	SAB(rs)b	10.44	-21.24	19.5 ^c	16/05/2013	B600-G5323	1800
NGC 4731	SB(s)cd	11.55	-18.92	13.2 ^c	11/05/2015	R831-G5322	3×865
NGC 4753	I0	10.85	-21.49	24.1 ^a	11/05/2015	B600-G5323	3×565
NGC 4818	SAB(rs)ab	11.89	-18.22	11.3 ^c	24/02/2017	B600-G5323	3×560
NGC 4902	SB(r)b	11.90	-20.82	32.4 ^b	03/02/2017	B600-G5323	3×560
NGC 4939	SA(s)bc	11.56	-21.39	42.5 ^c	14/02/2015	R831-G5322	3×865
NGC 4941	(R)SAB(r)ab	11.90	-19.72	21.2 ^t	09/02/2017	B600-G5323	3×560
NGC 4958	SB0(r)	11.48	-20.27	21.4 ^q	12/05/2015	B600-G5323	3×582
NGC 4984	(R)SAB0(rs)	11.71	-20.1	21.3 ^j	08/08/2016	B600-G5323	570
NGC 4995	SAB(rs)b	11.90	-20.1	23.4 ^c	02/03/2017	B600-G5323	3×560
NGC 5018	E3	11.71	-21.48	37.5 ^u	08/06/2013	B600-G5323	1800
NGC 5044	E0	11.92	-21.15	32.2 ^a	04/05/2013	B600-G5323	1800
NGC 5054	SA(s)bc	11.51	-20.04	18.2 ^c	29/04/2015	R831-G5322	3×865
NGC 5061	E0	11.35	-20.07	15.2 ^g	02/03/2015	B600-G5323	3×565
NGC 5068	SAB(rs)cd	10.53	-18.92	6.7 ^j	29/04/2015	R831-G5322	3×865
NGC 5101	(R)SB0/a(rs)	11.58	-19.73	14 ^g	11/05/2013	B600-G5323	1800
NGC 5102	SA0	10.64	-17.29	4 ⁱ	02/03/2015	B600-G5323	3×565
NGC 5128	S0	7.89	-19.75	3.53 ^v	29/04/2015	B600-G5323	3×565
NGC 5161	SA(s)c	11.98	-19.73	21.9 ^c	17/02/2018	R831-G5322	3×885
NGC 5170	SA(s)c	11.88	-20.43	27.5 ^c	09/03/2017	R831-G5322	3×870
NGC 5236	SAB(s)c	8.51	-20.95	4.79 ^w	23/02/2014	R831-G5322	3×815
NGC 5247	SA(s)bc	11.10	-21.06	22.2 ^j	29/04/2015	R831-G5322	3×865
NGC 5334	SB(rs)c	11.90	-20.46	32.6 ^x	10/03/2017	R831-G5322	3×875
NGC 5556	SAB(rs)d	11.88	-18.95	16.1 ^a	08/03/2017	R831-G5322	3×870
NGC 5584	SAB(rs)cd	11.95	-18.64	17.9 ^c	19/02/2018	R831-G5322	3×885
NGC 5643	SAB(rs)c	10.89	-20.7	16.9 ^j	22/02/2014	R831-G5322	3×815
NGC 6118	SA(s)cd	11.91	-19.71	20.7 ^c	27/02/2018	R831-G5322	3×885
NGC 6684	(R')SB0(s)	11.34	-19.55	13.6 ^a	30/04/2015	B600-G5323	3×565
NGC 6744	SAB(r)bc	9.24	-19.71	7.66 ^c	08/05/2014	R831-G5322	3×815
NGC 6868	E2	11.83	-21.47	34 ^g	04/05/2013	B600-G5323	1800
NGC 7049	SA0(s)	11.64	-21.46	29.9 ^a	11/05/2013	B600-G5323	1800
NGC 7090	SBc	11.10	-17.58	6.22 ^c	26/07/2015	R831-G5322	3×884
NGC 7144	E0	11.79	-20.25	24.4 ^a	24/07/2015	B600-G5323	3×565
NGC 7205	SA(s)bc	11.57	-19.85	18.3 ^c	09/08/2016	R831-G5322	3×861
NGC 7213	SA(s)a	11.18	-20.65	22 ^j	12/05/2015	B600-G5323	3×565
NGC 7410	SB(s)a	11.30	-21.91	44.1 ^c	12/05/2015	B600-G5323	3×565
NGC 7424	SAB(rs)cd	10.99	-19.89	11.5 ^j	23/09/2013	R831-G5322	3×808
NGC 7496	SB(s)b	11.78	-17.39	7.4 ^s	31/05/2017	B600-G5323	3×560
NGC 7507	E0	11.43	-21.52	24.6 ^a	10/08/2013	B600-G5323	1800

Object	Type	B	M_B	Distance (Mpc)	Obs. Date	Grating	Exp. Time (s)
NGC 7552	(R')SB(s)ab	11.40	-19.72	14.8 ^y	04/08/2017	B600-G5323	3×560
NGC 7582	(R')SB(s)ab	11.46	-20.48	22.5 ^a	17/07/2004	B600-G5323	3×720
NGC 7606	SA(s)b	11.55	-21.26	37.3 ^c	16/06/2016	B600-G5323	3×570
NGC 7713	SB(r)d	11.65	-18.33	9.25 ^c	13/07/2018	R831-G5322	3×885
NGC 7793	SA(s)d	9.65	-18.23	3.73 ^c	10/10/2016	R831-G5322	3×865
IC 1459	E3-4	10.96	-21.76	28.7 ^a	03/08/2008	B600-G5323	1800
IC 4296	E	11.58	-22.43	50.8 ^a	16/05/2013	B600-G5323	1800
IC 5201	SB(rs)cd	11.54	-18.44	10.5 ^c	12/05/2015	R831-G5322	3×865
IC 5267	SA0/a(s)	11.39	-20.95	24.5 ^g	16/05/2015	B600-G5323	3×582
IC 5273	SB(rs)cd	11.90	-19.12	15.5 ^c	01/07/2017	R831-G5322	3×870
IC 5328	E4	11.95	-20.93	39.7 ^g	08/08/2016	B600-G5323	3×570
SIFS							
NGC 150	SB(rs)b	11.75	-19.87	23.1 ^c	21/11/2019	700 l/mm	3×1200
NGC 210	SAB(s)b	11.65	-19.97	21.6 ^d	13/09/2018	700 l/mm	3×1200
NGC 578	SAB(rs)c	11.48	-19.62	18.1 ^c	26/11/2019	700 l/mm	3×1200
NGC 986	SB(rs)ab	11.80	-18.93	11.1 ^y	21/11/2019	700 l/mm	3×1200
NGC 1042	SAB(rs)cd	11.49	-16.44	4.2 ^β	27/11/2019	700 l/mm	3×1200
NGC 1087	SAB(rs)c	11.56	-19.17	12.9 ^c	27/11/2019	700 l/mm	3×1200
NGC 1232	SAB(rs)c	10.50	-20.2	14.5 ^f	23/11/2017	700 l/mm	3×1200
NGC 1350	(R')SB(r)ab	11.40	-20.44	19.7 ^c	13/09/2018	700 l/mm	3×1200
NGC 1371	SAB(rs)a	11.50	-21.13	30.3 ^c	21/11/2019	700 l/mm	3×1200
NGC 1385	SB(s)cd	11.65	-18.1	7.9 ^s	26/11/2019	700 l/mm	3×1200
NGC 1421	SAB(rs)bc	11.95	-19.6	19.2 ^c	23/11/2019	700 l/mm	3×1200
NGC 1425	SA(s)b	11.60	-20.6	22.5 ^c	26/11/2019	700 l/mm	3×1200
NGC 1448	SAcd	11.30	-19.67	17 ^c	23/11/2017	700 l/mm	3×1200
NGC 1493	SB(r)cd	11.82	-18.45	11.3 ^j	23/11/2019	700 l/mm	3×1200
NGC 1512	SB(r)a	11.38	-19.52	12.6 ^c	13/09/2018	700 l/mm	3×1200
NGC 1744	SB(s)d	11.70	-18.24	9.95 ^c	23/11/2019	700 l/mm	3×1200
NGC 1964	SAB(s)b	11.60	-20.2	23.7 ^c	26/11/2019	700 l/mm	3×1200
NGC 2090	SA(rs)c	11.85	-19.25	13.4 ^c	23/11/2019	700 l/mm	3×1200
NGC 4856	SB0/a(s)	11.40	-20.49	24 ^t	06/02/2017	700 l/mm	3×1200
NGC 5530	SA(rs)bc	11.98	-18.93	11.6 ^c	20/05/2018	700 l/mm	3×1200
NGC 6753	(R)SA(r)b	11.93	-20.34	23.4 ^g	20/05/2018	700 l/mm	3×1200
NGC 7083	SA(s)bc	11.80	-21.13	36 ^a	19/05/2018	700 l/mm	3×1200
NGC 7723	SB(r)b	11.85	-20.55	29.2 ^c	13/09/2018	700 l/mm	3×1200
NGC 7727	SAB(s)a	11.55	-20.26	19.7 ^b	13/09/2018	700 l/mm	3×1200
IC 5332	SA(s)d	11.25	-19.03	8.4 ^j	13/09/2018	700 l/mm	3×1200
Not Observed							
NGC 685	SAB(r)c	11.97	-19.02	15.2 ^j			
NGC 779	SAB(r)b	11.86	-19.69	20 ^c			
NGC 1084	SA(s)c	11.25	-20.23	17.4 ^c			
NGC 1249	SB(s)cd	11.80	-18.84	15.3 ^c			
NGC 1532	SB(s)b	11.53	-20.75	19.9 ^c			
NGC 1637	SAB(rs)c	11.52	-19.89	17.5 ^a			

Distances for the galaxies were obtained from: ^a - Tully et al. (2013), ^b - Bottinelli et al. (1984), ^c - Tully et al. (2016), ^d - Erwin & Debattista (2017), ^e - Tully et al. (2009), ^f - Nasonova et al. (2011), ^g - Springob et al. (2014), ^h - Blakeslee et al. (2001), ⁱ - Tonry et al. (2001), ^j - Tully & Fisher (1988), ^k - Cantiello et al. (2013), ^l - Springob et al. (2009), ^m - Blakeslee et al. (2010), ⁿ - Cantiello et al. (2005), ^o - Sabbi et al. (2018), ^p - Bottinelli et al. (1986), ^q - Theureau et al. (2007), ^r - Riess et al. (2016), ^s - Sorce et al. (2014), ^t - Karachentsev & Nasonova (2013), ^u - Ganeshalingam et al. (2013), ^v - Ferrarese et al. (2007), ^w - Pierce (1994), ^x - Karachentsev et al. (2014), ^y - Russell (2002), ^α - Jensen et al. (2003), ^β - Luo et al. (2016).

2 THE DIVING^{3D} SURVEY

In order to build the DIVING^{3D} sample, we selected all galaxies from RSA in the Southern hemisphere ($\delta < 0$) with $B < 12.0$ and $|b| > 15^\circ$. From this selection, 11 Sm/Im objects were excluded, since it was not possible to clearly identify their nuclei in the 2MASS images. The final sample has 170 objects and is shown in Table 1. It is worth mentioning that RSA is statistically complete for $B < 12.0$ (Sandage & Tammann 1981). Fig. 1 presents the distributions of the apparent and absolute B magnitudes, distances and morphological types for the final DIVING^{3D} sample. The references for the distances of the galaxies are shown in Table 1. The median distance of the objects in our sample is 19.0 Mpc. The apparent B magnitudes were taken from RSA. Whenever possible, the absolute B magnitudes, corrected for Galactic extinction, were obtained from the Carnegie-Irvine Galaxy Survey (CGS; Ho et al. 2011), or else from Hyperleda (Paturel et al. 2003). The median absolute B magnitude for the sample is -20.24 . The morphological types were taken from RC 3 (de Vaucouleurs et al. 1991) and they are distributed as follows: 30 ellipticals (18 per cent), 32 S0+S0/a (19 per cent), 16 Sa+Sab (9 per cent), 43 Sb+Sbc (25 per cent), 23 Sc (14 per cent) and 26 Scd+Sd (15 per cent). Bars are present in almost two thirds of the disc galaxies (S0 plus spirals).

A total of 131 galaxies were observed with the IFU of the Gemini Multi-Object Spectrograph (GMOS; Allington-Smith et al. 2002) at the 8 m Gemini South telescope. Eight galaxies were observed using the same instrument, but at the Gemini-North telescope. The observations were taken in the one-slit mode, which resulted in a field of view (FOV), sampled by 500 fibers (with a diameter of 0.2 arcsec each), of 5 arcsec \times 3.5 arcsec and in a sky FOV (at projected distance of 1 arcmin from the science FOV), sampled by 250 fibers, of 5 arcsec \times 1.75 arcsec.

The SOAR Integral Field Spectrograph (SIFS), at the 4 m SOAR telescope, was used to observe 25 galaxies from the sample. The fore-optics module of the instrument was set to produce a magnification of the image of 0.3 arcsec/fibre at the input of the IFU, resulting in a FOV of 7.8 arcsec \times 15 arcsec.

The GMOS/IFU and SIFS observations were all seeing limited. The median seeing values are 0.70 arcsec for the observations performed with GMOS/IFU and 1.04 arcsec for those obtained with SIFS. For the GMOS/IFU observations, we used field stars that are present in the acquisition image of the galaxy to estimate the seeing values. For SIFS, we also used acquisition images, but for the standard stars that were observed in the same night as the galaxies. We intend to observe the remaining six galaxies of the DIVING^{3D} sample with SIFS in the near future. It is worth emphasizing that, although this survey uses data obtained with GMOS/IFU and SIFS, such instruments provide very similar spectral coverages and spectral and spatial resolutions. Therefore, the use of these two instruments will not introduce significant biases in our analyses. Fig. 2 shows a histogram with the seeing values of all the observations taken with GMOS. More detail on the observations and data reduction of the DIVING^{3D} sample is presented in Section 3.1.

2.1 The scientific rationale

A distinguishing characteristic of the DIVING^{3D} survey, in comparison to other galaxy samples observed with IFUs, is the high spatial resolution. The idea is to have the highest possible spatial resolution and signal-to-noise ratio. Previous IFU surveys, such as CALIFA (Sánchez et al. 2012), SAURON (de Zeeuw et al. 2002), ATLAS^{3D} (Cappellari et al. 2011), SAMI (Bryant et al. 2015), S7 (Dopita et al. 2015; Thomas et al. 2017) and MaNGA (Bundy et al. 2015) were

able to spatially resolve phenomena that are all mixed up in Palomar and SDSS data. The DIVING^{3D} survey will, by contrast, map phenomena that are blurred in the data cubes of those surveys, i.e. physical processes in the nuclear and circumnuclear scales (100 pc) with a spatial resolution of ~ 20 pc. No other IFU survey is aiming at this sweet-spot region of galaxies, where high stellar and gaseous densities, high metallicities, presence of (active or dormant) SMBHs and other extreme conditions drive a variety of phenomena seen nowhere else in galaxies: ionization cones, obscuring tori, inflows and outflows, nuclear clusters, inner gaseous and stellar disks, etc. In Fig. 3, we present the spatial resolutions and the pixel scales of the DIVING^{3D} data in comparison to other IFU surveys.

Recently, some works have shown the importance of using IFU data with high spatial resolution in order to study some of these phenomena. For instance, Wylezalek et al. (2017) used both GMOS and MaNGA data cubes to study ionized gas outflows in two AGN hosts. In particular, in the object with lower bolometric luminosity, the outflow was only revealed using the GMOS data cube. Riffel et al. (2019) also used both GMOS and MaNGA data to characterize the prototype Red Geiser galaxy Akira. In this case, the GMOS data cube was important to detect a change of direction in the outflow from the inner part of the galaxy to kpc scales. In some other galaxies, a stellar kinematically decoupled core with scales of ~ 100 pc was only detected when high-spatial resolution data cubes were used as a complement to large FOV IFU observations (McDermid et al. 2006; Ricci et al. 2016). A systematic study of the circumnuclear regions using the DIVING^{3D} survey will be very important in order to characterize these structures from a statistical point of view.

The exquisite spatial resolution of the DIVING^{3D} survey will allow us to investigate the connection between AGNs and surrounding stellar populations to an unprecedented level of spatial detail, shedding new light on long-standing puzzles. For instance, while type 2 Seyferts show a clear tendency to host recent star-formation (Heckman et al. 1997; González Delgado et al. 2001; Cid Fernandes et al. 2001; Kauffmann et al. 2003), it is unclear whether this also happens in type 1 Seyferts. A natural extension of this topic is the co-evolution between the central SMBHs and their host galaxies, which is suggested by the existence of correlations between the masses of the SMBHs and parameters of the host galaxies. However, the existence and the way this co-evolution occurs are still uncertain. Kormendy & Ho (2013), for example, question whether low-mass galaxies follow a $M-\sigma$ relation and also argue that the co-evolution between the SMBHs and the host galaxies is probably more complex than suggested by the $M-\sigma$ relation. The feedback from AGNs seems to be an important component for the co-evolution of SMBHs and galaxies. Outflows generated by AGNs can shut off star formation in a ‘negative’ feedback (Fabian 2012). On the other hand, spatially resolved spectroscopic observations revealed that, in certain circumstances, AGN outflows can also trigger star formation in a ‘positive’ feedback (Maiolino et al. 2017; Gallagher et al. 2019). This, again, confirms that the role of the AGN in the possible co-evolution of SMBHs and the host galaxies is very complex. The DIVING^{3D} data will allow us to analyse, with high spatial and spectral resolution, the gas kinematics in the surroundings of the AGNs. We will be able to detect outflows and to determine connections between them and the star formation in these central regions of the galaxies (e.g. Diniz et al. 2017; Dahmer-Hahn et al. 2019b; da Silva et al. 2020b). The analysis of the stellar kinematics will reveal possible rotating stellar disks around the central SMBHs and, in certain cases, will allow us to estimate the masses of the central SMBHs (e.g. Menezes & Steiner 2015; Menezes et al. 2018; Ricci & Steiner 2020), which will result in contributions to studies related to the $M-\sigma$ relation.

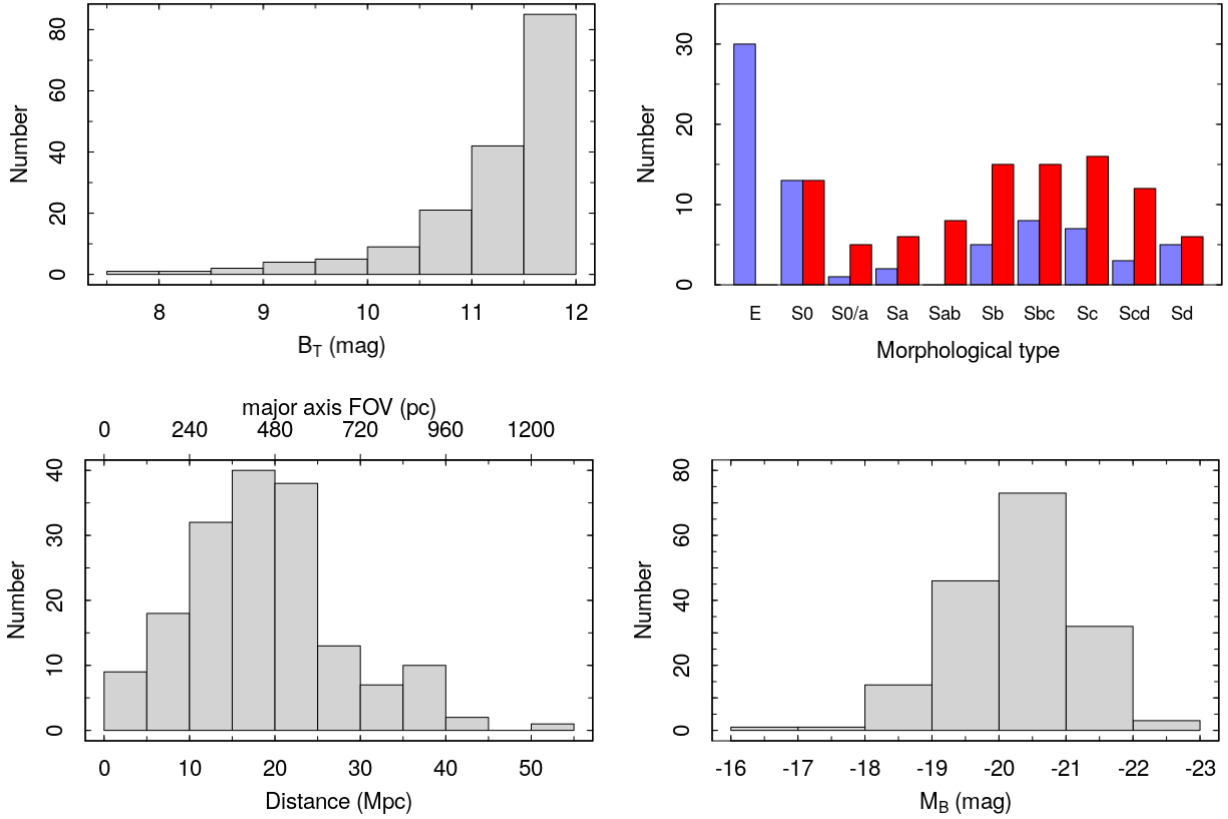


Figure 1. Basic properties of the DIVING^{3D} sample. Top left: distribution of apparent B magnitudes. Top right: distribution of morphological types. The purple bars correspond to unbarred galaxies and the red bars correspond to barred galaxies. Note that all elliptical galaxies of the sample do not have a bar and that all Sab galaxies have a bar, according to RC 3. Bottom left: distribution of distances, with a median value of 17.7 Mpc. Bottom right: distribution of absolute B magnitudes, with a median value of -20.06.

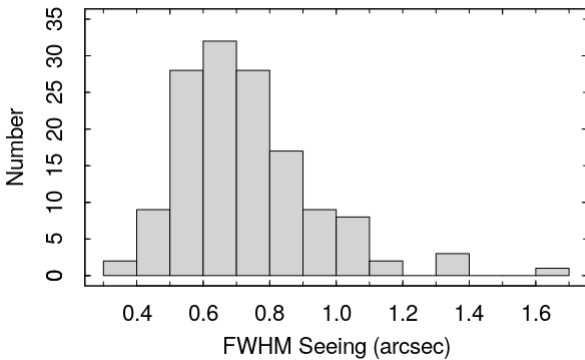


Figure 2. Distribution of the seeing values of all objects of the DIVING^{3D} sample that were observed with GMOS, with a median value of 0.70 arcsec.

The DIVING^{3D} may also shed a light on the census of LLAGNs. Most of the LLAGNs are LINERs (Ho 2008; Heckman & Best 2014) and their statistics is limited by the sensitivity of the detection techniques and by the spatial resolution of the observations, which is important in order to isolate the nuclear region from its surround-

ings. Some attempts to detect AGNs using IFU surveys, like MaNGA, were presented in the literature (see e.g. Wylezalek et al. 2018); however, the fraction of nuclear activity that is detected may be quite low, since the nebular emission that is powered by AGNs is diluted by the emission that is caused by other ionization processes, mainly because of the lower spatial resolution of the observations (Sánchez 2020). We believe that, with the techniques developed by our group (Steiner et al. 2009; Menezes 2012; Menezes et al. 2014a, 2015, 2019), together with the high spatial resolution of the DIVING^{3D} data, we will be able to detect AGNs at lower luminosity limits than the current level of detection. This belief is based on two facts: first, our preliminary results (see Section 4) indicate that we found a significantly higher number of objects with a broad $H\alpha$ component than anticipated from the Palomar survey. A second and perhaps more important argument comes from the $\log N - \log S$ analysis of AGNs present in Sc–Sd galaxies. There is a very strong tendency of such objects to appear in the nearest galaxies only. In X-rays, a larger proportion than expected has been detected, but the emission from X-ray binaries may affect the statistical analysis of LLAGNs (Desroches & Ho 2009). More reliable is the detection of [Ne v] at 14 and 24 μm (MIR) (Satyapal et al. 2008) that suggests that the presence of AGNs in late-type galaxies could be possibly 4 times higher than inferred at optical wavelengths.

LINERs also pose interesting questions. If star formation and

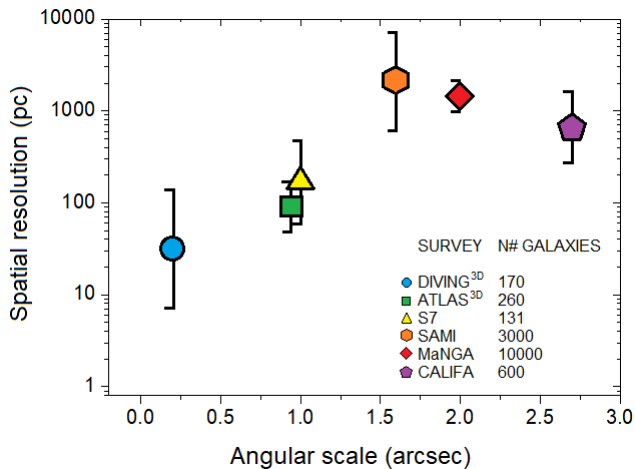


Figure 3. Diagram showing the angular scale of the instruments (fibre or image slicer sizes) and the spatial resolutions between the nearest and the farthest galaxies of some IFU galaxy surveys (within the vertical brackets "J"). The surveys are identified in the bottom right part of the diagram (namely, the ATLAS^{3D}, S7, SAMI, MaNGA, CALIFA) and are followed by their estimated number of observed galaxies. Since the angular resolutions of the DIVING^{3D} survey are limited by the seeing of the observations, we opted to use the median seeing of 0.7 arcsec to calculate its spatial resolution. The spatial resolutions of the other surveys are limited by the angular scale of the instruments. One may see that the data cubes of the DIVING^{3D} survey reach the highest spatial resolutions so far.

AGNs are indeed interconnected (possibly with a time delay due to AGN feedback quenching star formation), then the fact that LINERs reside among old stars poses a puzzle. Maybe the once young and luminous stars present in an earlier Seyfert phase dim to a level where they can no longer be detected in contrast to the much brighter bulge population, especially when observed through large apertures. Again, the spatial resolution of the DIVING^{3D} data, coupled to our sophisticated analysis techniques, will help identifying stellar population variations. Based on SDSS data, [Cid Fernandes et al. \(2011\)](#) proposed that LINERs containing true AGNs show some residual level of recent star formation in the last Gyr, while those LINERs where stars are all old are not truly AGNs, but retired galaxies ([Stasińska et al. 2008](#)), where the ionizing photon budget is dominated not by an AGN but HOLMES. With a much greater sensitivity to AGN signatures, the DIVING^{3D} survey will help disentangling true from fake AGNs.

The DIVING^{3D} survey will certainly contribute to studies related to the AGN luminosity function. [Ho \(2008\)](#) obtained a luminosity function for the H α emission line in AGNs, in the local universe, in the form of $\Phi \propto L^{-1.2 \pm 0.2}$. One of the sources of uncertainties for this luminosity function is the difficulty for differentiating true AGNs from impostors (LINERs powered by HOLMES and not by AGNs, for example). With the high spatial resolution of the DIVING^{3D} survey data, together with the benefits provided by our treatment and analysis techniques, we will be able to detect true AGNs in a more reliable way. To confirm the presence of an AGN in a given galaxy, we will first analyse its nuclear emission-line spectrum. If the emission-line ratios of this spectrum indicate a Seyfert, then we may confirm a true AGN. If the line ratios indicate a LINER, then we will search for a broad component in H α . If a broad component is present, we will check if it really comes from an unresolved source by making an image of the wing (usually the red wing) of the broad component. If no broad component is detected in the spectrum, then we will need to search

for other indicators of nuclear activity, such as the existence of X-ray or radio cores, or the presence of high-ionization lines in MIR spectra (e.g. the [O IV] and [Ne V] lines). Due to the selection criteria of our sample, only the AGN luminosity function in the local universe will be evaluated. Even so, the results may provide relevant information about the topic of the AGN evolution with z . It is currently accepted that the spatial density of more luminous AGNs increases with z and peaks at $z \sim 2$. This phenomenon is usually called AGN downsizing. For $z > 2$, the density of more luminous AGNs tends to slowly decrease ([Merloni & Heinz 2013](#)). The discussion of such a scenario depends also on a precise description of the AGN luminosity function at $z \sim 0$, for which the DIVING^{3D} survey will be able to contribute.

One additional relevant topic for the DIVING^{3D} survey is related to the so-called transition objects, which are usually interpreted as LINERs contaminated by the emission from H II regions ([Ho et al. 1993, 2003](#)). If that is the case, one would expect that observations with sufficiently high spatial resolution would be able to disentangle the emission from the central LINER from the putative circumnuclear H II regions and, as a consequence, the number of detected transition objects would decrease substantially. However, there is no consensus in the literature about this scenario for transition objects. [Shields et al. \(2007\)](#), for example, analysed high spatial resolution Space Telescope Imaging Spectrograph (STIS) data of 23 galaxies from the sample of the PALOMAR survey and did not find complete support for such a scenario. The DIVING^{3D} survey is intended to make a significant contribution to this topic, considering the high spatial resolution of the data.

2.2 The main DIVING^{3D} objectives

Our main goals with this project are:

1 – **Nuclear emission-line properties.** We aim to quantify, with high signal/noise and high (seeing-limited) spatial resolution, the properties of the nuclei of all galaxies in the sample. Our objective is to detect the faintest AGNs that can currently be observed in the optical. The diagnostic diagrams of these objects may show a decrease in the number of transition objects population as H II regions tend to be separated from LINERs/Seyferts.

2 – **Circumnuclear emission-line properties.** The circumnuclear emission can reveal aspects about ionizing sources that may be important within a scale of ~ 100 pc. Is the AGN responsible for the circumnuclear emission or are there other sources of excitation/ionization such as shock waves or HOLMES? We intend to identify structures, such as ionization cones, which should allow a test of whether the unified model ([Antonucci 1993; Urry & Padovani 1995](#)) applies to LLAGNs as well.

3 – **Central stellar and gas kinematics.** We will obtain not only information about rotating stellar and gas discs, but also about deviations from these patterns, such as counter-rotations, kinematically decoupled cores, gas inflows and outflows, etc. Whenever possible, we intend to estimate the masses of the central SMBHs and also the mass-to-light ratio (M/L), using gas and stellar kinematic parameters, which may be relevant for studies related to the M – σ relation ([Ferrarese & Merritt 2000; Gebhardt et al. 2000; Gültekin et al. 2009](#)).

4 – **Central stellar archaeology.** The spectral synthesis will always be attempted in order to perform the subtraction of the stellar continuum from the DIVING^{3D} data cubes. This is an essential step for a reliable analysis of the emission-line spectra of the objects. As a by-product, one may obtain information about the star-formation history (SFH) of the nucleus and of the circumnuclear environment.

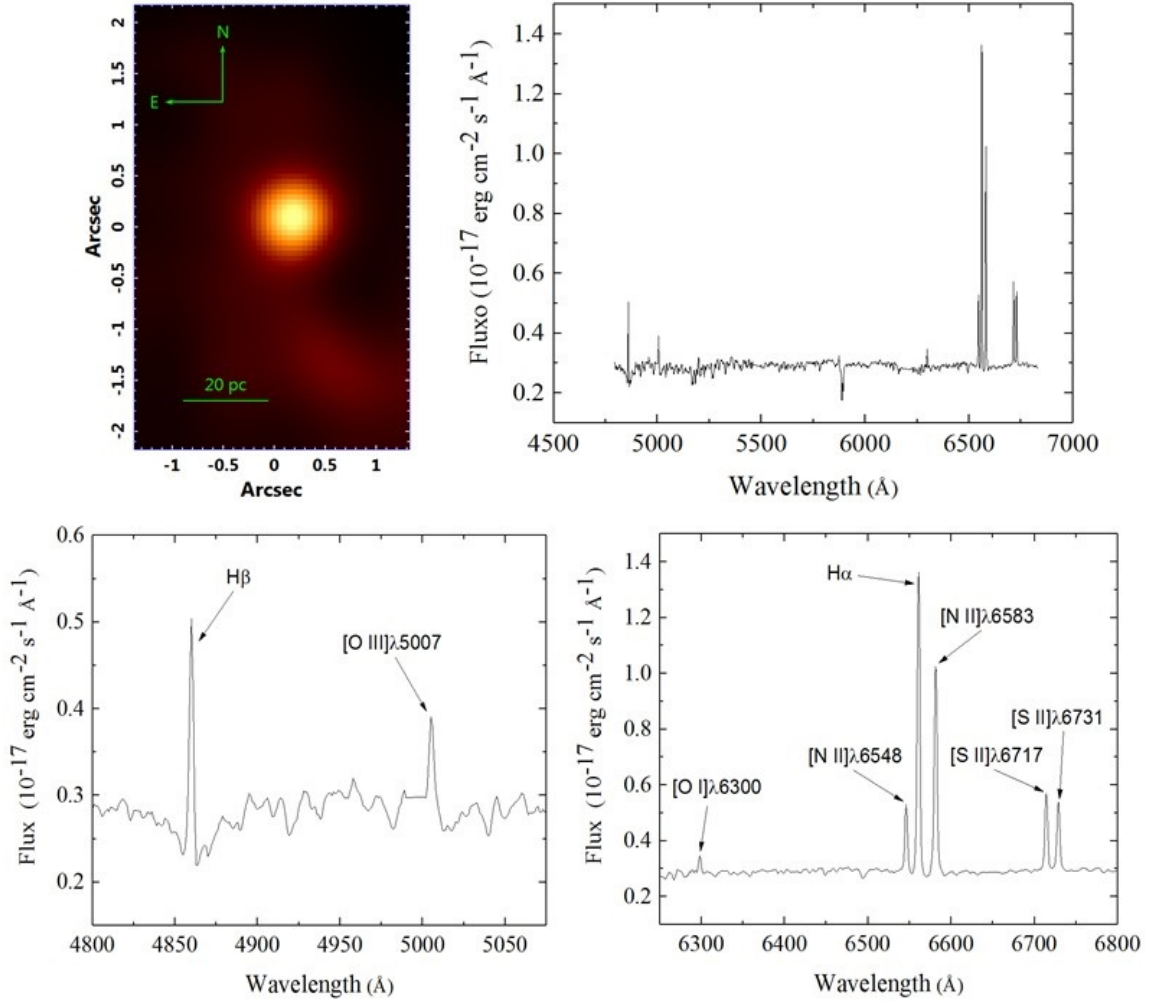


Figure 4. Image of the GMOS/IFU data cube of the central region of the galaxy NGC 5236, collapsed along the spectral axis, and its average spectrum. Magnifications of the average spectrum are shown at the bottom.

3 METHODOLOGIES FOR THE REDUCTION, TREATMENT AND ANALYSIS OF THE DATA

3.1 Data reduction and data treatment

The GMOS/IFU observations of ETGs, with morphological types E, S0 - Sb, were taken with the B600 grating, which provided a wavelength coverage of 4250 - 7000 Å and a spectral resolution of 1.8 Å, measured with the sky emission line of [O I]λ5577. On the other hand, late-type galaxies, with morphological types Sbc - Sd, were observed with the R831 grating, resulting in a wavelength coverage of 4800 - 6890 Å and in a spectral resolution of 1.3 Å, measured with the sky emission line of [O I]λ5577. We opted to use the R831 grating for the observations of late-type galaxies due to their lower masses and, therefore, their lower values of the stellar velocity dispersion. As a consequence, a grating with a higher spectral resolution, such as R831, would allow a more accurate analysis of the stellar kinematics in these objects. The analysis of the stellar kinematics in higher mass ETGs, on the other hand, does not require such a high spectral resolution. Therefore, in these cases, we opted to use the B600 grating, with a longer wavelength coverage, which resulted in more accurate results obtained with stellar archaeology (see Section 3.4).

For most of the objects, three exposures, with a spatial dithering of 0.2 arcsec per dither step, were taken, centred on the peak of the stellar

emission of the galaxies. For certain objects, just one exposure, without spatial dithering, was taken. The GMOS/IFU data were reduced using the Gemini package, in IRAF environment. Bias, GCAL-flat, twilight-flat and CuAr lamp calibration images were obtained for each galaxy. A spectrophotometric standard star was also observed for each observing programme. The first step of the data reduction consisted of a simple trimming and overscan and bias subtraction. We also applied the L. A. Cosmic routine (van Dokkum 2001) for the removal of cosmic rays from the data. Then, a correction of bad pixels was performed, using a bad pixel mask obtained from the GCAL-flat images, and the spectra were extracted. Response maps obtained from the twilight-flat images were used to correct for gain variations between the fibres. Response curves provided by the GCAL-flat images were also used to correct for gain variations between the spectral pixels. The next step in the data reduction was the wavelength calibration, using the CuAr lamp images. The sky emission was subtracted using the average spectrum of the sky FOV. Since the DIVING^{3D} sample includes nearby galaxies, there was a possibility of the sky FOV in the GMOS/IFU (located at a projected distance of 1' from the science FOV) be contaminated by the galaxy emission. In order to avoid this problem, we performed a cross-correlation between the science spectra and the sky spectra for each object in the sample, searching for spectral features of the observed galaxy in the sky FOV.

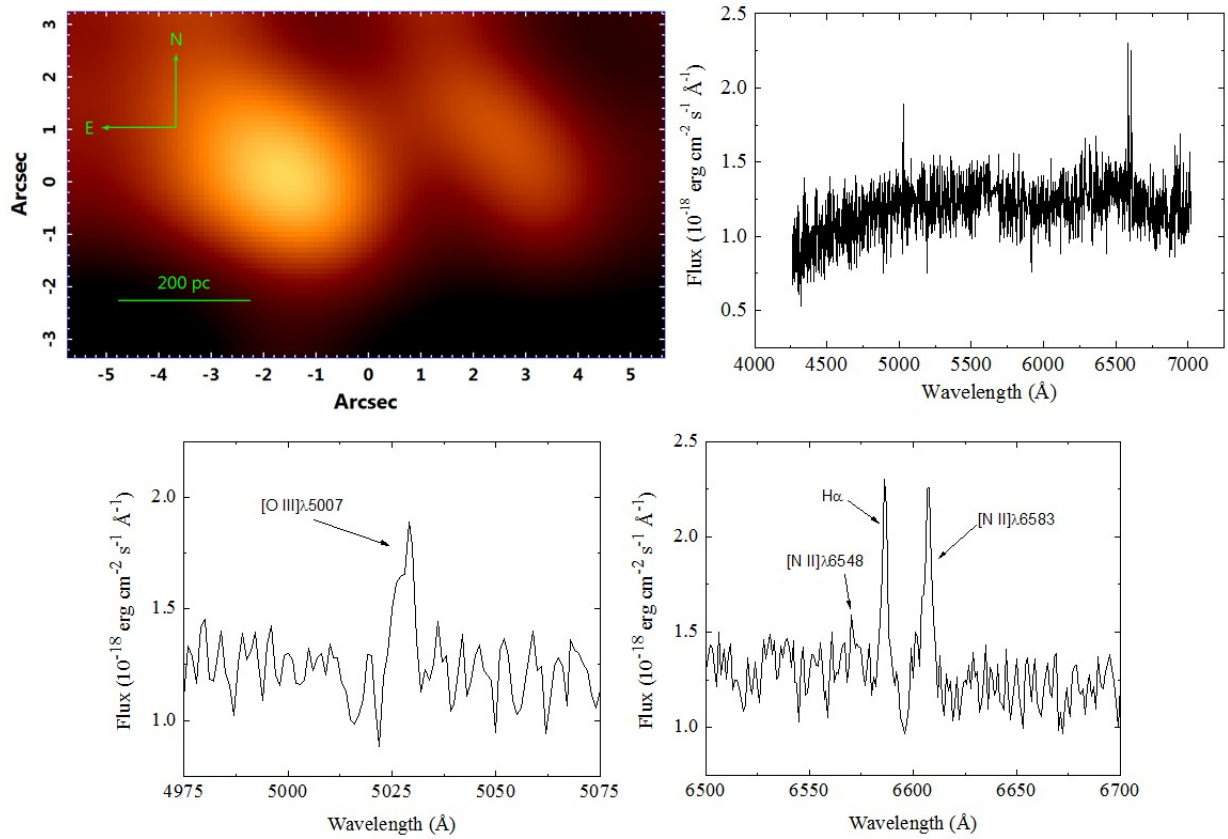


Figure 5. Image of the SIFS data cube of the central region of the galaxy NGC 1448, collapsed along the spectral axis, and its average spectrum. Magnifications of the average spectrum are shown at the bottom.

NGC 5236

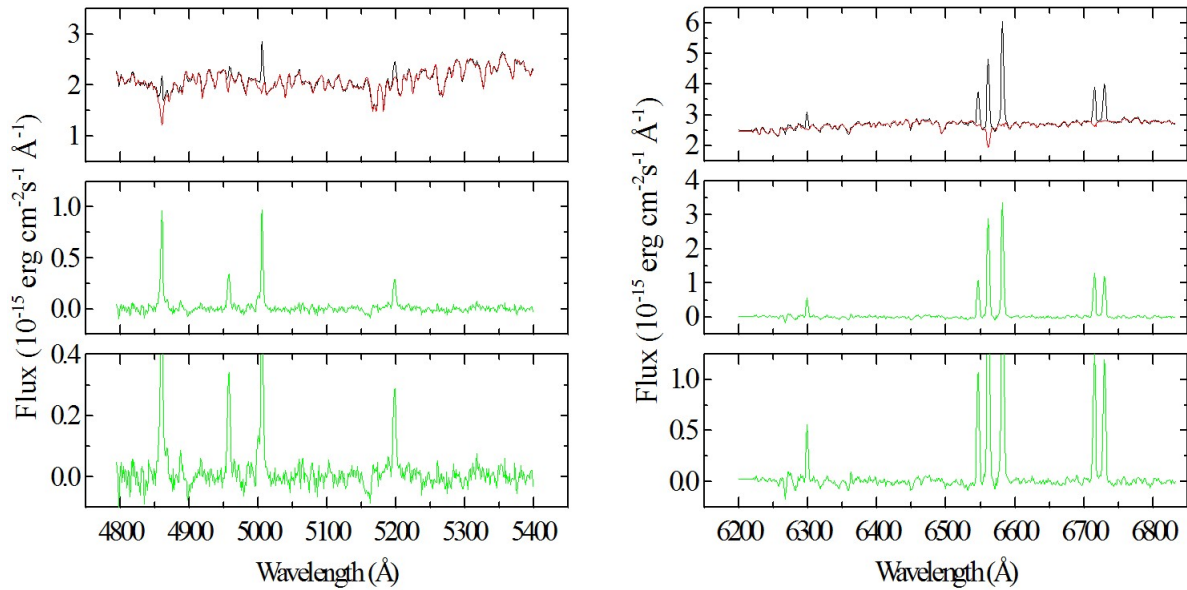


Figure 6. Spectrum extracted from the nucleus of the galaxy NGC 5236. The observed spectrum is shown in black, the fit provided by the pPXF technique is shown in red and the fit residuals are shown in green.

NGC 4594

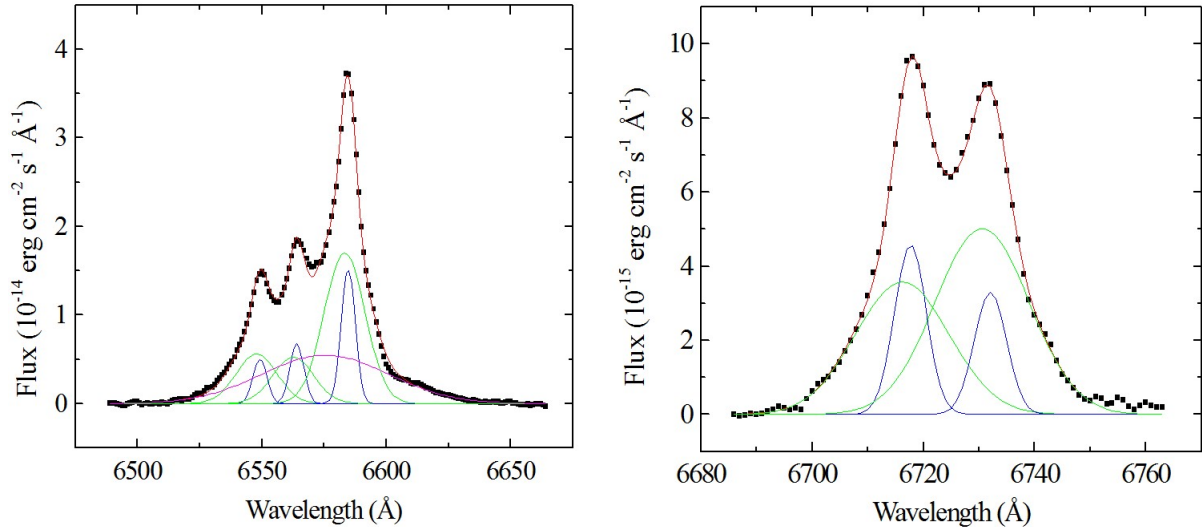


Figure 7. Gaussian fits applied to the [S II] and [N II]+H α emission lines of the nuclear spectrum of NGC 4594. The green and blue curves correspond to the narrow components of the emission lines, the magenta curve represents the broad component of the H α emission line and the red curve corresponds to the final fit.

For all the galaxies in the sample observed with GMOS/IFU, such features were not detected. After the sky subtraction, the data were flux calibrated, taking into account the atmospheric extinction, using the observed spectrophotometric standard stars. Finally, the last step was the construction of data cubes, with spaxels of 0.05 arcsec.

The SIFS observations were taken with a grating of 700 l/mm, providing a spectral coverage of 4500 - 7300 Å and a spectral resolution of 1.3 Å, measured with the sky emission line of [O I] λ 5577. Six exposures, with a spatial dithering of 0.3 arcsec per dither step, were obtained for the central region of the galaxy. The data reduction was performed using scripts in Interactive Data Language (IDL). Bias, flat, milky-flat, HgAr and spectrophotometric standard stars calibration images were obtained for the observing night. Similarly to the case of GMOS/IFU data, the first step of the SIFS data reduction was a simple trimming and bias and overscan subtraction. The science image was then divided by the normalized milky-flat image (which is essentially a flat-field image with a degraded focus), in order to correct for gain variations between pixels. After that, the spectra were extracted and, using the flat image, a correction for gain variations between the fibres was applied. The data were wavelength calibrated, using the HgAr images. SIFS has also a FOV, separated from the science FOV, for the observation of the sky emission. The average spectrum of such a sky FOV was subtracted from the science spectra. We used the cross-correlation technique described before to check for possible contaminations of the sky spectra by the galaxy emission. However, no such a contamination was detected so far in the objects in the DIVING^{3D} sample observed with SIFS. Finally, the data were flux calibrated, taking into account the atmospheric extinction, using the spectrophotometric standard star observed at the same night, and data cubes were constructed, with spaxels of 0.3 arcsec.

After the data reduction, a data treatment was applied to all data cubes. The treatment procedure used for the GMOS/IFU data cubes is described in detail in Menezes et al. (2019) and included: correction of the differential atmospheric refraction (DAR); combination of the data cubes of each galaxy into one in the form of a median, to

remove remaining cosmic rays and bad pixels not removed during the data reduction; Butterworth spatial filtering, to remove high spatial frequency noise from the images of the data cubes; “instrumental fingerprint” removal, which is essential, as this instrumental feature (usually presenting a low-frequency spectral signature and appearing as horizontal or vertical stripes across the images) can significantly compromise the analyses to be performed; and Richardson-Lucy deconvolution, to improve the spatial resolution of the data cubes. In the case of SIFS data cubes, the treatment procedure was similar, except that the DAR correction was not applied because SOAR has an Atmospheric Dispersion Corrector and, as a consequence, the obtained data cubes do not show the DAR effect. For more detail about the data treatment procedure, see Menezes et al. (2014a, 2015). Fig. 4 shows, as an example, the image of the GMOS/IFU data cube of the central region of the galaxy NGC 5236, collapsed along the spectral axis, together with its average spectrum. Fig. 5 shows the same, but for the SIFS data cube of the galaxy NGC 1448.

3.2 Analysis of the emission-line spectra

For a reliable analysis of the emission-line spectra of the data cubes, we first apply a subtraction of the stellar continuum using synthetic stellar spectra provided by the Penalized Pixel Fitting (pPXF) procedure (Cappellari & Emsellem 2004), which is performed by fitting the observed stellar spectra with combinations of template stellar population spectra, from a given base, convolved with a Gauss-Hermite expansion. Fig. 6 shows the fit provided by the pPXF technique applied to a spectrum extracted from the data cube of NGC 5236. The fit residuals, which represent the emission-line spectrum, are also shown.

Emission lines are analysed in terms of Gaussian decomposition. Normally, this procedure consists of fitting the [S II] and the [N II]+H α emission lines with a two-kinematic component model. However, in certain cases, a single-kinematic component model is used. In order to reproduce a possible broad component of the H α emission line, a broad Gaussian function is added to the model, when

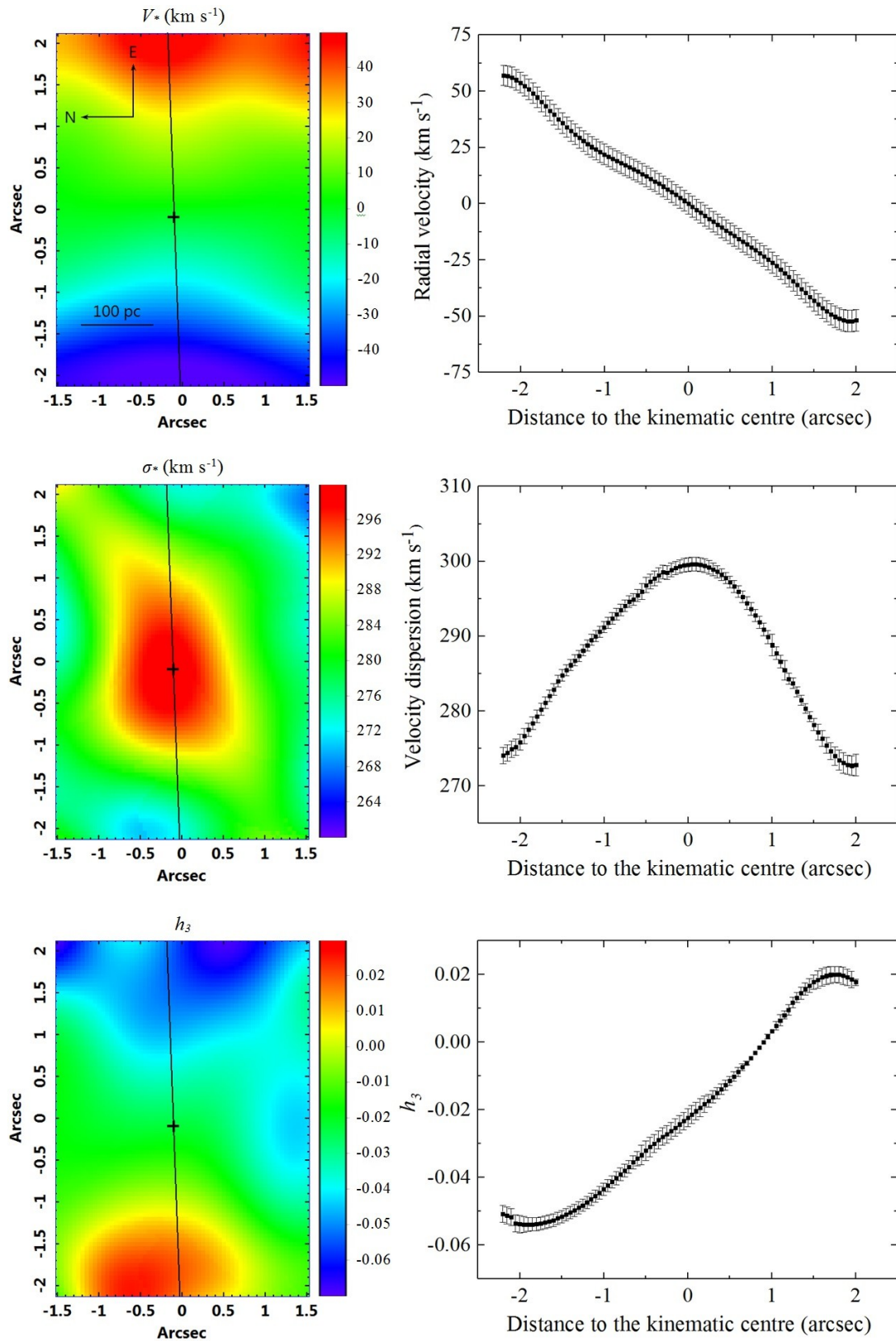


Figure 8. Maps of V_* , σ_* and of the Gauss-Hermite coefficient h_3 obtained with the pPXF technique applied to the GMOS/IFU data cube of the central region of NGC 1395. The curves of each map extracted from the axis corresponding to the line of nodes of the V_* map, represented by the black line, are shown on the right. The kinematic centre of the V_* map, corresponding to the black cross, was taken as the point, along the line of nodes, at which the velocity was equal to the average between the maximum and minimum velocities. Such average velocity was subtracted from the V_* map, which shows then the velocity values relative to the kinematic centre.

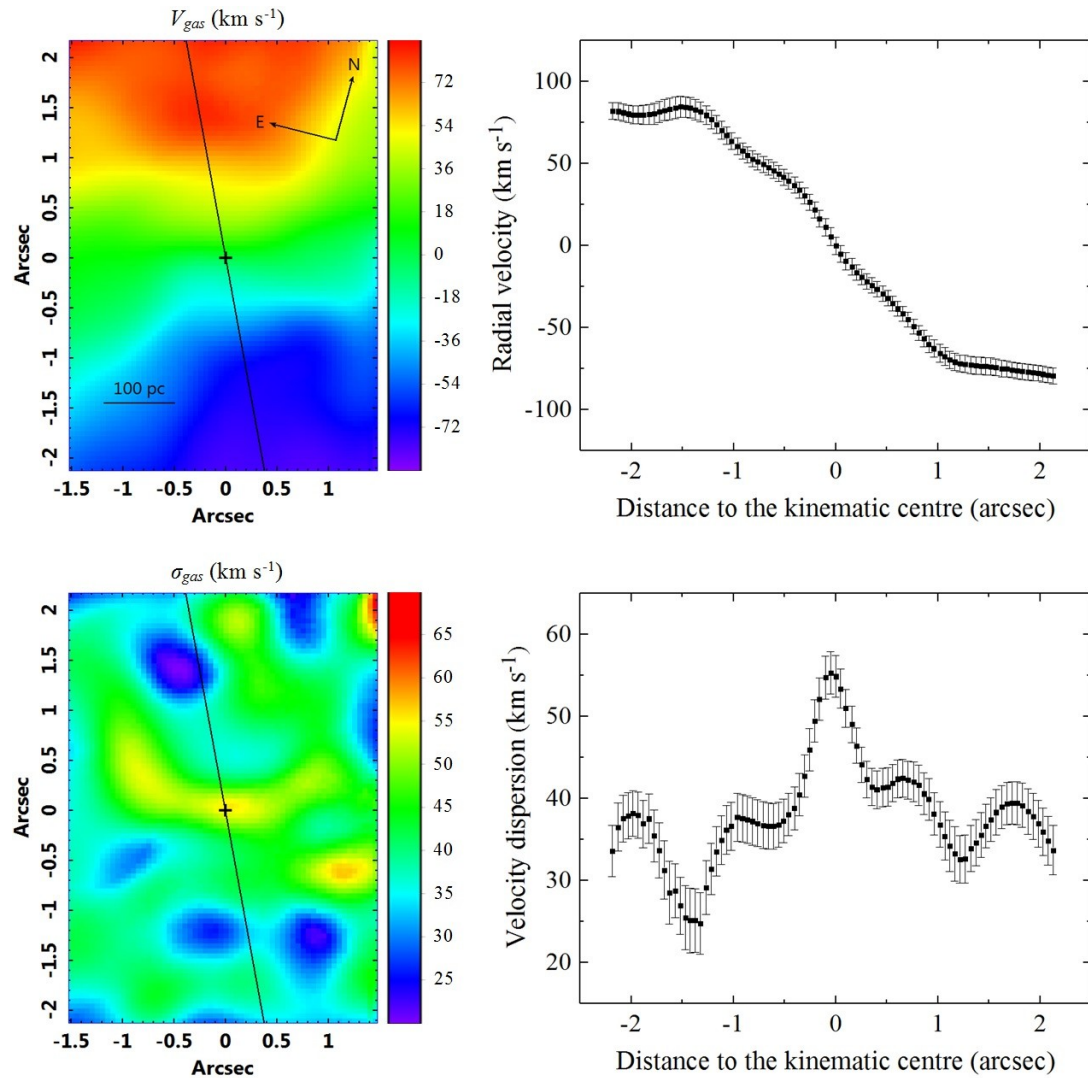


Figure 9. Maps of V_{gas} and σ_{gas} obtained by fitting the $[\text{N II}]+\text{H}\alpha$ emission lines, in the data cube of the central region of NGC 1395, with a sum of three Gaussian functions with the same width and radial velocity. The curves of each map, extracted from the axis corresponding to the line of nodes of the V_{gas} map, represented by the black line, are shown on the right. The kinematic centre of the V_{gas} map, corresponding to the black cross, was taken as the point, along the line of nodes, at which the velocity was equal to the average between the maximum and minimum velocities. Such average velocity was subtracted from the V_{gas} map, which shows then the velocity values relative to the kinematic centre.

necessary. By applying this process, we are able to determine the flux ratios of the narrow components of different emission lines. Diagnostic diagrams (Baldwin et al. 1981; Veilleux & Osterbrock 1987) are used to classify the emission-line spectra of the data cubes as being characteristic of LINERs, Seyferts, transition objects or H II regions. Such a procedure is applied to both nuclear and circumnuclear regions of the galaxies. Fig. 7 shows the Gaussian fits applied to the $[\text{S II}]$ and $[\text{N II}]+\text{H}\alpha$ emission lines of the nuclear spectrum of NGC 4594.

3.3 Analysis of the stellar and gas kinematics

The pPXF technique also provides parameters related to the stellar kinematics, such as the stellar radial velocity (V_*), the stellar velocity dispersion (σ_*) and the Gauss-Hermite coefficients. Since this procedure is applied to the spectrum corresponding to each spaxel of the data cubes, we obtain maps of all these kinematic parameters. Fig. 8

shows the maps of the stellar kinematic parameters of the data cube of the galaxy NGC 1395. The gas kinematic parameters are obtained by fitting Gaussian functions to the main emission lines of the spectra, such as the $[\text{N II}]+\text{H}\alpha$ emission lines. Again, since the Gaussian fits are applied to the spectrum corresponding to each spaxel of the data cubes, the results are maps of the gas kinematic parameters. Fig. 9 shows maps of the gas radial velocity (V_{gas}) and of the gas velocity dispersion (σ_{gas}) of the data cube of NGC 1395.

3.4 Stellar archaeology

The stellar archaeology parameters can be derived by means of the STARLIGHT spectral synthesis code (Cid Fernandes et al. 2005), similarly to what was done for galaxy-wide data cubes in the CALIFA project (e.g., Pérez et al. 2013; Cid Fernandes et al. 2013; González Delgado et al. 2014). Fig. 10 shows example maps of light-weighted mean age, dust optical depth and stellar mass surface density for the

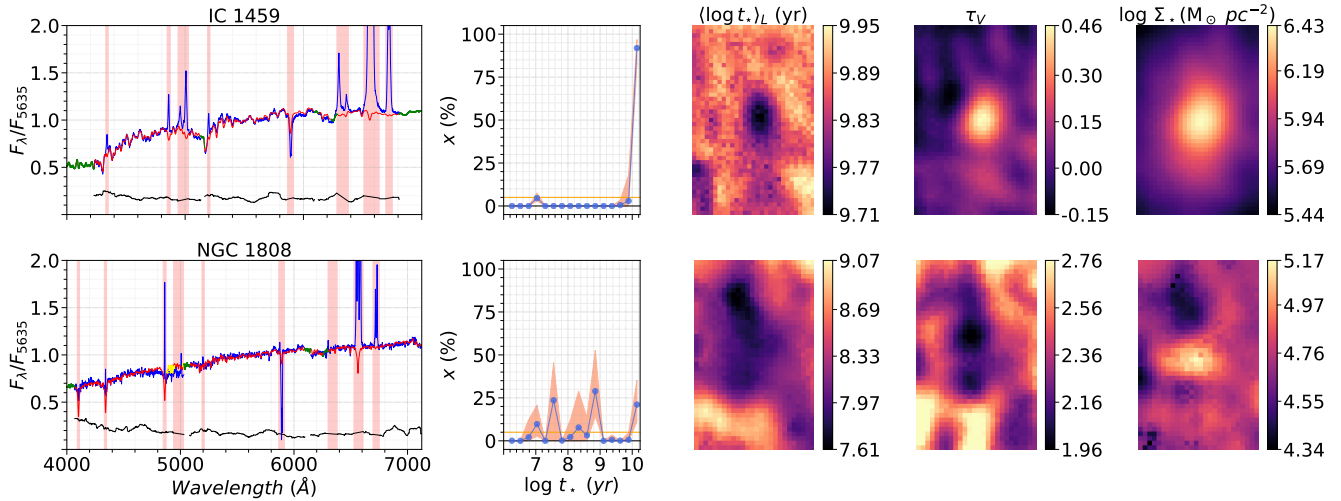


Figure 10. Stellar population properties derived with `STARLIGHT` for the elliptical galaxy IC 1459 (*top*) and the spiral galaxy NGC 1808 (*bottom*). The first panel shows the observed spectrum (blue), the best-fitting model (red) and the error spectrum (black). Green portions of the spectrum indicate regions without data or bad pixels and red areas are masked regions. Second panel is the SFH. The blue curve is the mean light fraction in each base component measured over the data cube. The areas in red indicate the 10-95th percentile range and the horizontal orange line is a visual reference for 5 per cent of the light fraction. The following three panels are the maps of light-weighted mean age, extinction and stellar mass surface density, respectively.

elliptical galaxy IC 1459 (top panels) and for the spiral galaxy NGC 1808 (bottom). The plot also shows the spectral fits and the derived light fractions (at 5635 Å) associated with populations of different ages.

One should note that the spectral coverage of `DIVING3D` does not include the blue/near-ultraviolet region of the spectrum, which contains important indicators of the age and metallicity of stellar populations (Leonardi & Rose 1996; Worthey & Ottaviani 1997; Trager et al. 1998). This limitation translates to difficulties and possibly biases in the inferred stellar population properties. Indeed, experiments carried out by Carvalho (2019) show that the light-weighted mean ages derived from data in the 4500-7000 Å spectral range tend to be younger than those obtained using a wider 3700-7000 Å window – see also Wolf et al. (2007), Cid Fernandes et al. (2014) and Gonçalves et al. (2020) for related experiments.

Nuclear activity itself is another complicating factor for stellar archaeology work. In some cases the amount of emission lines (which are masked from the spectral fits) in the nuclear region leave little room for a reliable stellar population analysis, as `STARLIGHT` has few or no strong absorption lines to anchor the fit. Furthermore, one should also allow for the presence of a non-stellar continuum. NGC 1566 is a good example of these issues. The analysis of the `DIVING3D` data cube of this galaxy by da Silva et al. (2017) found a $f_V \propto \nu^{-1.7}$ in the nuclear region ($r < 0.5$ arcsec).

Despite these caveats, our previous experience (e.g. da Silva et al. 2017, 2018; Menezes & Steiner 2018; da Silva et al. 2020b) show that this process can, at least, differentiate, with good precision, emission from young and old stars and also detect differences in the metallicities of the stellar populations.

4 EARLY RESULTS

To date 20 papers showing specific analyses of `DIVING3D` data have already been published. Studies (focused on the line-emitting regions, the stellar and gas kinematics and the stellar archaeology) of

the central regions of six individual galaxies of the `DIVING3D` sample resulted in the following publications: NGC 4594 (Menezes et al. 2013), NGC 1313 (Menezes & Steiner 2017), NGC 5044 (Diniz et al. 2017), NGC 7582 (Ricci et al. 2018), NGC 1052 (Dahmer-Hahn et al. 2019a,b) and NGC 2835 (Menezes et al. 2019). In certain objects, peculiar features were detected, such as an off-centred AGN in NGC 3115 (Menezes et al. 2014b), a compact off-centred Seyfert emission (with a deficit of emission at the AGN position) in NGC 3621 (Menezes et al. 2016), double stellar nuclei in NGC 908 and NGC 1187 (Menezes & Steiner 2018) and a double-peaked $H\alpha$ emission in NGC 4958 (Ricci & Steiner 2019).

One of the subsamples of the `DIVING3D` includes the Milky Way morphological twins (da Silva 2016, 2020). Five papers about the analyses of individual objects of such a subsample were already published. The first (da Silva et al. 2017) was focused on the Seyfert 1 nucleus of NGC 1566. The second (da Silva et al. 2018) presented the analysis of the central region of NGC 6744, a nucleus with old stellar populations and LINER emission. The other three papers described the rich environments in the central regions, with LINER emission, of NGC 613 (da Silva et al. 2020a,b) and NGC 2442 (da Silva et al. 2021).

Five ETGs that belong to the `DIVING3D` survey were part of a sample of 10 massive ETGs from the local Universe, all observed with GMOS/IFU using the same setup as the `DIVING3D` objects (Ricci 2013; Ricci et al. 2014a). LINER-like nuclei were detected in all 10 objects (Ricci et al. 2014b), with six of them being type-1 AGNs. In addition, Ricci et al. (2015) studied the properties of the extended emission of these objects and proposed a model for LINER-like circumnuclear regions where the emission along gas disks are caused by an extended-ionization source, probably HOLMES, while the emission in the direction perpendicular to the disks are related to a low-velocity ionization cone where the ionizing photons from the AGN are collimated by some agent aligned with the gas disk. Finally, Ricci et al. (2016) studied the stellar kinematic properties of this sample. Seven galaxies have a rotation structure within their central region, i.e. in a scale of ~ 100 pc. In NGC 1404, which is part

of the DIVING^{3D} survey, a kinematic decoupled core was clearly detected. This series of papers will serve as a guide to the analysis that will be performed in the ETG subsample of the DIVING^{3D} survey.

Regarding the statistical results, a preliminary analysis of the subsample of ETGs in the DIVING^{3D} survey revealed that 91 per cent of these objects show nuclear emission lines (Ricci et al. 2021). In addition, the nuclear emission-line spectra of 50 per cent of the ETGs are typical of LINERs and Seyferts (31 per cent are actually type 1 AGNs). The analysis of the subsample of galaxies brighter than $B=11.2$ (which we call mini-DIVING^{3D} sample; Menezes et al. 2021, Menezes et al. in preparation) reveals similar results, with 93 per cent of the objects with nuclear emission lines and 50 per cent showing emission-line spectra typical of LINERs or Seyferts. One interesting point is that the diagnostic diagram analysis of the mini-DIVING^{3D} sample indicates an apparent dichotomy between H II regions and LINERs/Seyferts, with few transition objects. This suggests that at least part of the transition objects are LINERs contaminated by the emission from H II regions and the high spatial resolution of the DIVING^{3D} data allows a more accurate separation between the nuclear and circumnuclear emission, resulting in a lower number of transition objects.

5 SUMMARY

We are conducting the DIVING^{3D} survey, which has the goal of analysing, using optical 3D spectroscopy, the central regions of all galaxies in the Southern hemisphere with $B < 12.0$ and $|b| > 15^\circ$. The complete sample has a total of 170 objects. From this sample, 131 galaxies were observed with the GMOS/IFU, at the Gemini South telescope, eight were observed also with GMOS/IFU but at the Gemini North telescope and 25 were observed with SIFS, at the SOAR telescope. It is intended that the remaining six galaxies will be observed with SIFS in the near future. The data obtained for this survey has a combination of high spatial and spectral resolutions not matched by previous surveys and will result in significant contributions to different research areas, such as the statistics of LLAGNs for galaxies with different morphological types, the ionization mechanisms in LINERs, the nature of transition objects, etc. The main objectives of the DIVING^{3D} survey are the study of: nuclear emission-line properties; circumnuclear emission-line properties; central stellar and gas kinematics; and central stellar archaeology.

The survey already resulted in 20 published papers, showing the analyses of the central regions of individual objects or small subsamples of the DIVING^{3D} survey. The first statistical results of the DIVING^{3D} survey, which are based on the analysis of the nuclear region of all galaxies of the sample with $B < 11.2$ (the mini-DIVING^{3D} sample), are presented in the second paper of this series (Menezes et al, submitted, but see also Menezes et al. 2021 for preliminary results on this sample). A summary containing preliminary results of the nuclear region of all ETGs of the DIVING^{3D} survey is presented in Ricci et al. (2021); a more complete analysis on the nuclear emission from the ETGs is in preparation. A statistical study of the Milky Way morphological twins of the sample is expected to be published in the near future. When all the objects of the DIVING^{3D} survey are observed, we intend to perform statistical studies of the complete sample and also of other subsamples, including, for example, the early spiral galaxies (Sa+Sab+Sb+Sbc) or the late spiral galaxies (Sc+Scd+Sd).

ACKNOWLEDGEMENTS

This work is dedicated to the memory of the founder of this survey, Prof. Dr. João Evangelista Steiner, who sadly passed away on 2020 September 10.

Based on observations obtained at the Gemini Observatory (processed using the Gemini IRAF package), which is operated by the Association of Universities for Research in Astronomy, Inc., under a cooperative agreement with the NSF on behalf of the Gemini partnership: the National Science Foundation (United States), the National Research Council (Canada), CONICYT (Chile), the Australian Research Council (Australia), Ministério da Ciência, Tecnologia e Inovação (Brazil) and Ministerio de Ciencia, Tecnología e Innovación Productiva (Argentina). This research has made use of the NASA/IPAC Extragalactic Database (NED), which is operated by the Jet Propulsion Laboratory, California Institute of Technology, under contract with the National Aeronautics and Space Administration. This research has also made use of the Carnegie-Irvine Galaxy Survey (<https://cgs.obs.carnegiescience.edu/CGS/Home.html>), the Hyperleda (<http://leda.univ-lyon1.fr/>) and RC3 (<https://heasarc.gsfc.nasa.gov/W3Browse/all/rc3.html>) databases. We thank Conselho Nacional de Desenvolvimento Científico e Tecnológico (CNPq) for support under grants 306063/2019-0 (RBM), 306790/2019-0 (TVR) and 141766/2016-6 (PS) and Fundação de Amparo à Pesquisa do Estado de São Paulo (FAPESP) - for support under grants 2011/51680-6 and 2020/13315-3 (PS). NVA acknowledges support of the Royal Society and the Newton Fund via the award of a Royal Society–Newton Advanced Fellowship (grant NAFR1\180403), and of Fundação de Amparo à Pesquisa e Inovação de Santa Catarina (FAPESC). We also thank an anonymous referee for valuable comments about this paper.

DATA AVAILABILITY

Further detail about the DIVING^{3D} survey can be found at <https://diving3d.maua.br>. The raw GMOS/IFU data are available at the Gemini Science Archive (<https://archive.gemini.edu/searchform>). The treated GMOS/IFU and SIFS data cubes can be requested at diving3d@gmail.com.

REFERENCES

- Allington-Smith J., et al., 2002, *PASP*, 114, 892
 Antonucci R., 1993, *ARA&A*, 31, 473
 Baldwin J. A., Phillips M. M., Terlevich R., 1981, *PASP*, 93, 5
 Bekki K., Graham A. W., 2010, *ApJ*, 714, L313
 Belfiore F., et al., 2016, *MNRAS*, 461, 3111
 Binette L., Magris C. G., Stasińska G., Bruzual A. G., 1994, *A&A*, 292, 13
 Blakeslee J. P., Lucey J. R., Barris B. J., Hudson M. J., Tonry J. L., 2001, *MNRAS*, 327, 1004
 Blakeslee J. P., et al., 2010, *ApJ*, 724, 657
 Bottinelli L., Gouguenheim L., Paturel G., de Vaucouleurs G., 1984, *A&AS*, 56, 381
 Bottinelli L., Gouguenheim L., Paturel G., Teerikorpi P., 1986, *A&A*, 156, 157
 Bryant J. J., et al., 2015, *MNRAS*, 447, 2857
 Bundy K., et al., 2015, *ApJ*, 798, 7
 Cantiello M., Blakeslee J. P., Raimondo G., Mei S., Brocato E., Capaccioli M., 2005, *ApJ*, 634, 239
 Cantiello M., et al., 2013, *A&A*, 552, A106
 Cappellari M., Emsellem E., 2004, *PASP*, 116, 138
 Cappellari M., et al., 2011, *MNRAS*, 413, 813
 Carvalho M. S., 2019, PhD thesis, Universidade Federal de Santa Catarina

- Cazzoli S., et al., 2018, *MNRAS*, **480**, 1106
- Cid Fernandes R., Heckman T., Schmitt H., González Delgado R. M., Storchi-Bergmann T., 2001, *ApJ*, **558**, 81
- Cid Fernandes R., Mateus A., Sodré L., Stasińska G., Gomes J. M., 2005, *MNRAS*, **358**, 363
- Cid Fernandes R., Stasińska G., Mateus A., Vale Asari N., 2011, *MNRAS*, **413**, 1687
- Cid Fernandes R., et al., 2013, *A&A*, **557**, A86
- Cid Fernandes R., et al., 2014, *A&A*, **561**, A130
- Dahmer-Hahn L. G., et al., 2019a, *MNRAS*, **482**, 5211
- Dahmer-Hahn L. G., et al., 2019b, *MNRAS*, **489**, 5653
- Desroches L.-B., Ho L. C., 2009, *ApJ*, **690**, 267
- Diniz S. I. F., Pastoriza M. G., Hernandez-Jimenez J. A., Riffel R., Ricci T. V., Steiner J. E., Riffel R. A., 2017, *MNRAS*, **470**, 1703
- Dopita M. A., et al., 2015, *ApJS*, **217**, 12
- Dudik R. P., Satyapal S., Marcu D., 2009, *ApJ*, **691**, 1501
- Eracleous M., Hwang J. A., Flohic H. M. L. G., 2010, *ApJ*, **711**, 796
- Erwin P., Debattista V. P., 2017, *MNRAS*, **468**, 2058
- Fabian A. C., 2012, *ARA&A*, **50**, 455
- Ferland G. J., Netzer H., 1983, *ApJ*, **264**, 105
- Ferrarese L., Merritt D., 2000, *ApJ*, **539**, L9
- Ferrarese L., Mould J. R., Stetson P. B., Tonry J. L., Blakeslee J. P., Ajhar E. A., 2007, *ApJ*, **654**, 186
- Filippenko A. V., Sargent W. L. W., 1985, *ApJS*, **57**, 503
- Flores-Fajardo N., Morisset C., Stasińska G., Binette L., 2011, *MNRAS*, **415**, 2182
- Gallagher R., Maiolino R., Belfiore F., Drory N., Riffel R., Riffel R. A., 2019, *MNRAS*, **485**, 3409
- Ganeshalingam M., Li W., Filippenko A. V., 2013, *MNRAS*, **433**, 2240
- Gebhardt K., et al., 2000, *ApJ*, **539**, L13
- Gonçalves G., Coelho P., Schiavon R., Usher C., 2020, *MNRAS*, **499**, 2327
- González Delgado R. M., Heckman T., Leitherer C., 2001, *ApJ*, **546**, 845
- González Delgado R. M., et al., 2014, *ApJ*, **791**, L16
- González-Martín O., Masegosa J., Márquez I., Guainazzi M., Jiménez-Bailón E., 2009, *A&A*, **506**, 1107
- Granato G. L., De Zotti G., Silva L., Bressan A., Danese L., 2004, *ApJ*, **600**, 580
- Gültekin K., et al., 2009, *ApJ*, **698**, 198
- Halpern J. P., Steiner J. E., 1983, *ApJ*, **269**, L37
- Heckman T. M., 1980, *A&A*, **500**, 187
- Heckman T. M., Best P. N., 2014, *ARA&A*, **52**, 589
- Heckman T. M., González-Delgado R., Leitherer C., Meurer G. R., Krolik J., Wilson A. S., Koratkar A., Kinney A., 1997, *ApJ*, **482**, 114
- Ho L. C., 2008, *ARA&A*, **46**, 475
- Ho L. C., Filippenko A. V., Sargent W. L. W., 1993, *ApJ*, **417**, 63
- Ho L. C., Filippenko A. V., Sargent W. L. W., Peng C. Y., 1997, *ApJS*, **112**, 391
- Ho L. C., Filippenko A. V., Sargent W. L. W., 2003, *ApJ*, **583**, 159
- Ho L. C., Li Z.-Y., Barth A. J., Seigar M. S., Peng C. Y., 2011, *ApJS*, **197**, 21
- Hopkins P. F., Hernquist L., 2006, *ApJS*, **166**, 1
- Jensen J. B., Tonry J. L., Barris B. J., Thompson R. I., Liu M. C., Rieke M. J., Ajhar E. A., Blakeslee J. P., 2003, *ApJ*, **583**, 712
- Karachentsev I. D., Nasonova O. G., 2013, *MNRAS*, **429**, 2677
- Karachentsev I. D., Karachentseva V. E., Nasonova O. G., 2014, *Astrophysics*, **57**, 457
- Kauffmann G., et al., 2003, *MNRAS*, **346**, 1055
- Kormendy J., Ho L. C., 2013, *ARA&A*, **51**, 511
- Leonardi A. J., Rose J. A., 1996, *AJ*, **111**, 182
- Luo R., Hao L., Blanc G. A., Jooe S., van den Bosch R. C. E., Weinzirl T., 2016, *ApJ*, **823**, 85
- Maiolino R., et al., 2017, *Nature*, **544**, 202
- Maoz D., Filippenko A. V., Ho L. C., Rix H.-W., Bahcall J. N., Schneider D. P., Macchetto F. D., 1995, *ApJ*, **440**, 91
- Masegosa J., Márquez I., Ramirez A., González-Martín O., 2011, *A&A*, **527**, A23
- McDermid R. M., et al., 2006, *MNRAS*, **373**, 906
- Menezes R. B., 2012, PhD thesis, Universidade de São Paulo
- Menezes R. B., Steiner J. E., 2015, *ApJ*, **808**, 27
- Menezes R. B., Steiner J. E., 2017, *MNRAS*, **466**, 749
- Menezes R. B., Steiner J. E., 2018, *ApJ*, **868**, 67
- Menezes R. B., Steiner J. E., Ricci T. V., 2013, *ApJ*, **765**, L40
- Menezes R. B., Steiner J. E., Ricci T. V., 2014a, *MNRAS*, **438**, 2597
- Menezes R. B., Steiner J. E., Ricci T. V., 2014b, *ApJ*, **796**, L13
- Menezes R. B., da Silva P., Ricci T. V., Steiner J. E., May D., Borges B. W., 2015, *MNRAS*, **450**, 369
- Menezes R. B., Steiner J. E., da Silva P., 2016, *ApJ*, **817**, 150
- Menezes R. B., da Silva P., Steiner J. E., 2018, *MNRAS*, **473**, 2198
- Menezes R. B., Ricci T. V., Steiner J. E., da Silva P., Ferrari F., Borges B. W., 2019, *MNRAS*, **483**, 3700
- Menezes R. B., Steiner J. E., Ricci T. V., da Silva P., Nicolazzi D. M., 2021, *IAU Symposium*, **359**, 450
- Merloni A., Heinz S., 2013, *Planets, Stars and Stellar Systems*, p. 503–566
- Nagar N. M., Falcke H., Wilson A. S., 2005, *A&A*, **435**, 521
- Nasonova O. G., de Freitas Pacheco J. A., Karachentsev I. D., 2011, *A&A*, **532**, A104
- Netzer H., 2013, The Physics and Evolution of Active Galactic Nuclei
- Neumayer N., Walcher C. J., 2012, *Advances in Astronomy*, **2012**, 709038
- Paturel G., Petit C., Prugniel P., Theureau G., Rousseau J., Brouty M., Dubois P., Cambrésy L., 2003, *A&A*, **412**, 45
- Pérez E., et al., 2013, *ApJ*, **764**, L1
- Phillips M. M., Jenkins C. R., Dopita M. A., Sadler E. M., Binette L., 1986, *AJ*, **91**, 1062
- Pierce M. J., 1994, *ApJ*, **430**, 53
- Ricci T. V., 2013, PhD thesis, Universidade de São Paulo
- Ricci T. V., Steiner J. E., 2019, *MNRAS*, **486**, 1138
- Ricci T. V., Steiner J. E., 2020, *MNRAS*, **495**, 2620
- Ricci T. V., Steiner J. E., Menezes R. B., 2014a, *MNRAS*, **440**, 2419
- Ricci T. V., Steiner J. E., Menezes R. B., 2014b, *MNRAS*, **440**, 2442
- Ricci T. V., Steiner J. E., Menezes R. B., 2015, *MNRAS*, **451**, 3728
- Ricci T. V., Steiner J. E., Menezes R. B., 2016, *MNRAS*, **463**, 3860
- Ricci T. V., Steiner J. E., May D., Garcia-Rissmann A., Menezes R. B., 2018, *MNRAS*, **473**, 5334
- Ricci T. V., Steiner J. E., Menezes R. B., 2021, *IAU Symposium*, **359**, 454
- Riess A. G., et al., 2016, *ApJ*, **826**, 56
- Riffel R. A., et al., 2019, *MNRAS*, **485**, 5590
- Russell D. G., 2002, *ApJ*, **565**, 681
- Sabbi E., et al., 2018, *ApJS*, **235**, 23
- Sánchez S. F., 2020, *ARA&A*, **58**, 99
- Sánchez S. F., et al., 2012, *A&A*, **538**, A8
- Sandage A., Tammann G. A., 1981, A Revised Shapley-Ames Catalog of Bright Galaxies
- Sarzi M., et al., 2010, *MNRAS*, **402**, 2187
- Satyapal S., Vega D., Dudik R. P., Abel N. P., Heckman T., 2008, *ApJ*, **677**, 926
- Shields J. C., et al., 2007, *ApJ*, **654**, 125
- Singh R., et al., 2013, *A&A*, **558**, A43
- Sorce J. G., Tully R. B., Courtois H. M., Jarrett T. H., Neill J. D., Shaya E. J., 2014, *MNRAS*, **444**, 527
- Springel V., Di Matteo T., Hernquist L., 2005, *MNRAS*, **361**, 776
- Springob C. M., Masters K. L., Haynes M. P., Giovanelli R., Marinoni C., 2009, *ApJS*, **182**, 474
- Springob C. M., et al., 2014, *MNRAS*, **445**, 2677
- Stasińska G., et al., 2008, *MNRAS*, **391**, L29
- Steiner J. E., Menezes R. B., Ricci T. V., Oliveira A. S., 2009, *MNRAS*, **395**, 64
- Theureau G., Hanski M. O., Coudreau N., Hallet N., Martin J. M., 2007, *A&A*, **465**, 71
- Thomas A. D., et al., 2017, *ApJS*, **232**, 11
- Tonry J. L., Dressler A., Blakeslee J. P., Ajhar E. A., Fletcher A. B., Luppino G. A., Metzger M. R., Moore C. B., 2001, *ApJ*, **546**, 681
- Trager S. C., Worthey G., Faber S. M., Burstein D., González J. J., 1998, *ApJS*, **116**, 1
- Tully R. B., Fisher J. R., 1988, Catalog of Nearby Galaxies
- Tully R. B., Rizzi L., Shaya E. J., Courtois H. M., Makarov D. I., Jacobs B. A., 2009, *AJ*, **138**, 323
- Tully R. B., et al., 2013, *AJ*, **146**, 86

- Tully R. B., Courtois H. M., Sorce J. G., 2016, *AJ*, 152, 50
- Urry C. M., Padovani P., 1995, *PASP*, 107, 803
- Veilleux S., Osterbrock D. E., 1987, *ApJS*, 63, 295
- Walcher C. J., Böker T., Charlot S., Ho L. C., Rix H. W., Rossa J., Shields J. C., van der Marel R. P., 2006, *ApJ*, 649, 692
- Wolf M. J., Drory N., Gebhardt K., Hill G. J., 2007, *ApJ*, 655, 179
- Worthey G., Ottaviani D. L., 1997, *ApJS*, 111, 377
- Wylezalek D., et al., 2017, *MNRAS*, 467, 2612
- Wylezalek D., Zakamska N. L., Greene J. E., Riffel R. A., Drory N., Andrews B. H., Merloni A., Thomas D., 2018, *MNRAS*, 474, 1499
- Yan R., Blanton M. R., 2012, *ApJ*, 747, 61
- da Silva P., 2016, Master's thesis, Universidade de São Paulo
- da Silva P., 2020, PhD thesis, Universidade de São Paulo
- da Silva P., Steiner J. E., Menezes R. B., 2017, *MNRAS*, 470, 3850
- da Silva P., Steiner J. E., Menezes R. B., 2018, *ApJ*, 861, 83
- da Silva P., Menezes R. B., Steiner J. E., 2020a, *MNRAS*, 492, 5121
- da Silva P., Menezes R. B., Steiner J. E., Fraga L., 2020b, *MNRAS*, 496, 943
- da Silva P., Menezes R. B., Díaz Y., López-Navas E., Steiner J. E., 2021, *MNRAS*, 505, 223
- de Vaucouleurs G., de Vaucouleurs A., Corwin Herold G. J., Buta R. J., Paturel G., Fouque P., 1991, Third Reference Catalogue of Bright Galaxies
- de Zeeuw P. T., et al., 2002, *MNRAS*, 329, 513
- van Dokkum P. G., 2001, *PASP*, 113, 1420

This paper has been typeset from a $\text{\TeX}/\text{\LaTeX}$ file prepared by the author.